Supporting Information Appendix

1. **Supporting Text.** Silica-rich terrestrial deposits without tridymite.

2. **Table S1**. Chemical compositions from Rietveld analysis and chemical composition of minerals used for calculation of summed chemical composition of crystalline material.

3. **Fig. S1. (a)** Elevation map of Gale crater showing location of geologic map (white box). **(b)** Geologic map with principal stratigraphic units.

4. **Fig. S2.** Generalized stratigraphy of bedrock exposed across Aeolis Palus (Bradbury group) and the lower part of Mt. Sharp (Murray formation).

5. **Fig. S3**. Comparison of Buckskin patterns from the summation of diffraction images 1-4 and 16-45.

6. **Fig. S4.** Individual diffraction patterns for each Buckskin crystalline mineral and fit (sum of individual mineral patterns).

7. **Fig. S5.** Diffraction patterns for the sum of amorphous and instrumental components, their individual patterns, and the Buckskin diffraction pattern.

8. **Fig. S6.** Transmission XRD patterns for high-silica amorphous materials.

Silica-rich terrestrial deposits without tridymite.

High-SiO$_2$ terrestrial environments where tridymite does not occur because sufficiently high temperatures are not present include hydrothermal and cryogenic silica sinter deposits (61-70). After initial deposition as colloidal opal-A, sinters undergo incremental and progressive mineralogical transformation in the sequence opal-A $\rightarrow$ opal-CT $\rightarrow$ opal-C $\rightarrow$ quartz with aging. Similarly, tridymite formation has not been reported in low temperature acid sulfate environments. Leaching of surface and near surface silicate country rock (New Zealand geothermal fields) by acid-sulfate steam produces high-SiO$_2$ residues, with the first-formed phase described as "disordered opal-A" (63, 69). The mineralogical aging sequence for the silica residues is described as opal-A $\rightarrow$ opal-CT $\rightarrow$ chalcedonic quartz. The maturation process was investigated experimentally at higher temperatures and pressures (430 °C and 31 MPa and circum-neutral pH) with silica polymorphs forming in the sequence amorphous-SiO$_2$ $\rightarrow$ cristobalite $\rightarrow$ quartz (70). In a field experiment, (65) reported that maturation of opal-A to quartz can be accelerated by acidic-steam condensate (pH = 3.5 – 5.5 and T = 74 – 94 °C).

Another type of high-SiO$_2$ deposit without reported tridymite is the hydrocarbon-bearing Athel Silicilyte (South Oman Salt Basin, Sultanate of Oman). This finely laminated sedimentary rock (mudstone) with up to 95 wt.% SiO$_2$ is interpreted (71, 72) as primary chemical precipitates of silica dissolved in evaporating seawater brines at temperatures too low (below 45 °C) for tridymite formation. Although the initial SiO$_2$ precipitate was likely colloidal or opaline silica, the Oman silicilyte is now chert (microcrystalline quartz) (72).

Table S1. Mineral compositions from Rietveld analysis and literature sources used for calculation of the summed chemical composition of Buckskin crystalline material.

	Tridymite	Cristobalite	Plagioclase	Sanidine	Magnetite	Anhydrite
*Buckskin Mineral Compositions Calculated from Unit Cell Parameters**						
Composition	---	---	$An_{41\pm8}Ab_{59\pm8}$	$Ab_{32\pm32}Or_{68\pm32}$	$Fe_{2.78\pm0.10}O_4$	---
Mineral Compositions Used for Calculation of Amorphous Material Chemical Composition[†]						
SiO_2 (wt.%)	96.5±3.7	100.0	55.7±0.9	65.7	---	---
TiO_2	0.4±0.7	---	---	---	---	---
Al_2O_3	1.6±2.3	---	27.7±0.6	18.6	---	---
Cr_2O_3	---	---	---	---	---	---
FeO	---	---	---	---	11.4	---
Fe_2O_3	0.3±0.2	---	0.6±0.4	---	88.6	---
MnO	---	---	---	---	---	---
MgO	0.4±0.1	---	0.1±0.1	---	---	---
CaO	0.3±0.3	---	10.3±0.6	---	---	41.2
Na_2O	0.6±0.5	---	5.5±0.4	2.8	---	---
K_2O	0.3±0.6	---	0.4±0.3	12.9	---	---
P_2O_5	---	---	---	---	---	---
SO_3	---	---	---	---	---	58.8
Cl	---	---	---	---	---	---
Total	100.4	100.0	100.3	100.0	100.0	100.0
Composition	---	---	$An_{50\pm3}Ab_{48\pm2}Or_{3\pm2}$	$Ab_{25}Or_{75}$	$Fe_{2.78\pm0.10}O_4$	$CaSO_4$
wt.% Crystalline	34.1±2.0	6.0±0.8	42.8±3.0	8.4±1.8	6.9±0.8	1.8±0.6

*Uncertainties are 2σ.

[†]Tridymite from average of (13, 14); plagioclase from average high SiO_2 martian meteorites (15); sanidine from Webmineral (http://www.webmineral.com/); magnetite from refined unit cell parameters assuming only Fe^{2+} and Fe^{3+} are present (cation-deficient magnetite); cristobalite and anhydrite from stoichiometric compositions; no detected crystalline mineral has Cr_2O_3, MnO, P_2O_5, and Cl so that their concentrations in bulk sample are assigned to the Buckskin amorphous material; weight percentages of minerals in crystalline material are from Table 2.
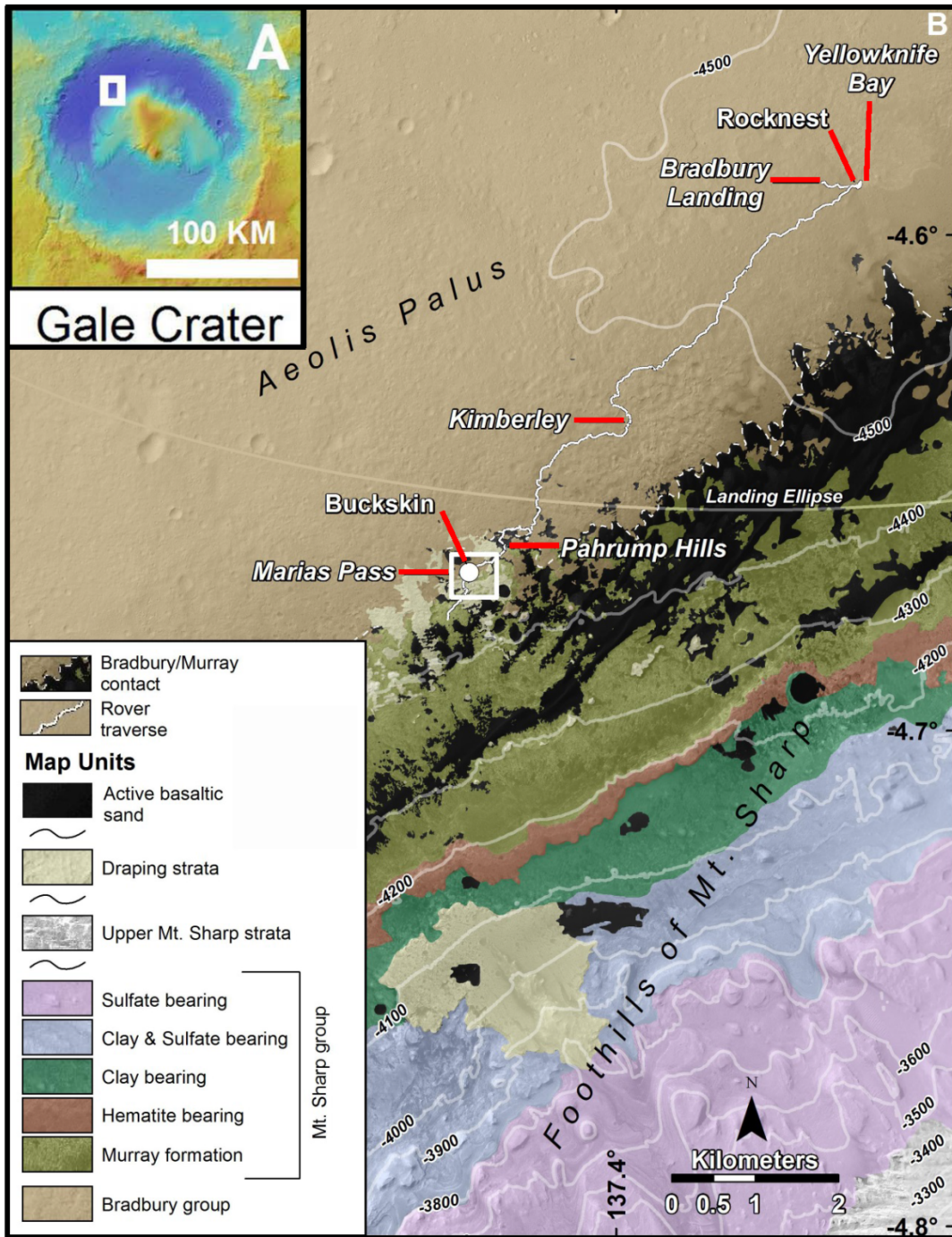
Fig. S1. (A) Elevation map of Gale crater showing location of Geologic map (white box). **(B)** Geologic map with principal stratigraphic units of Aeolis Palus (Bradbury group) and foothills of Mt. Sharp (Murray formation), major study locations (Rocknest, Yellowknife Bay, Kimberley, Pahrump Hills, and Marias Pass), rover traverse, and landing ellipse. The Buckskin drill hole is located in the Marias Pass area (white box).
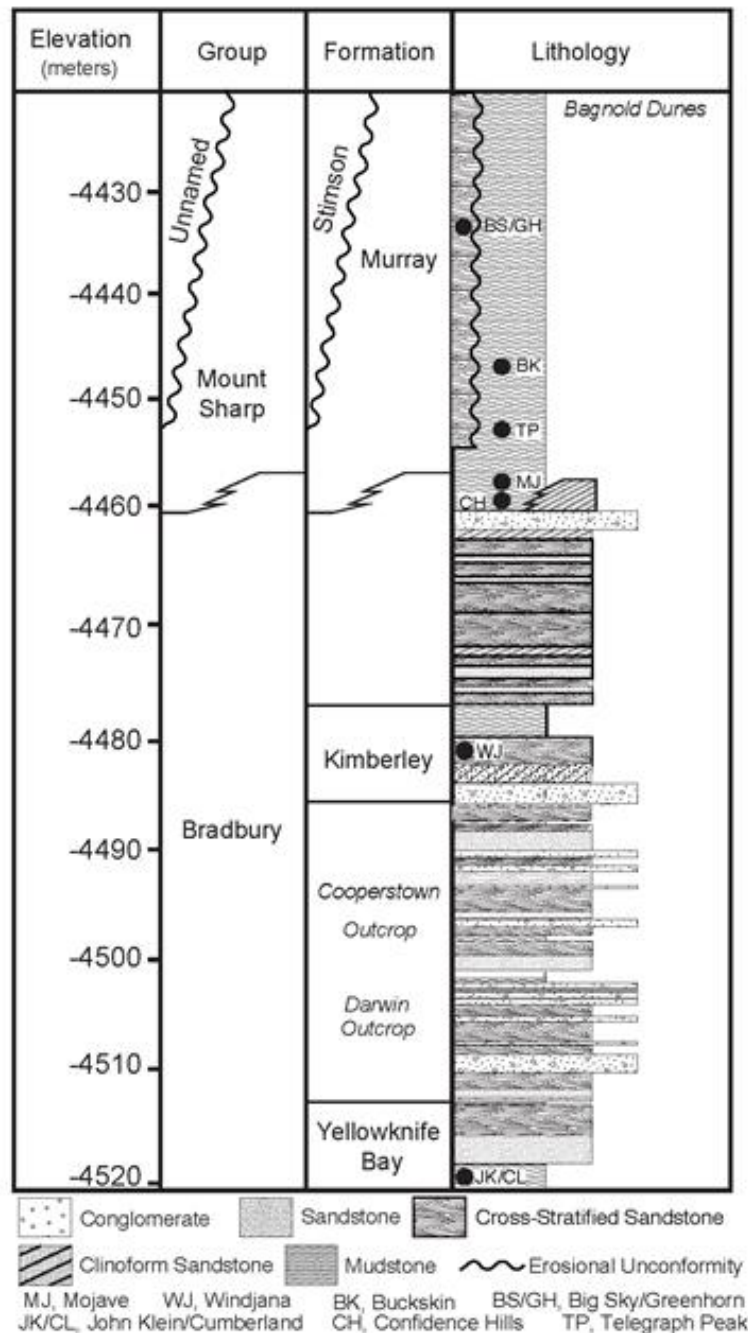
Fig. S2. Generalized stratigraphy of bedrock exposed across Aeolis Palus (Bradbury group) and the lower part of Mt. Sharp (Murray formation). See (1) for more detailed breakdown of depositional facies, and their interpretation as fluvial and lacustrine deposits. Drill holes are indicated by JK (John Klein) and CB (Cumberland) at Yellowknife Bay, WJ (Windjana) at Kimberley, CH (Confidence Hills), MJ (Mojave) and TP (Telegraph Peak) at Pahrump Hills, and BK (Buckskin) at Marias Pass. See Fig. S1 for geologic map.
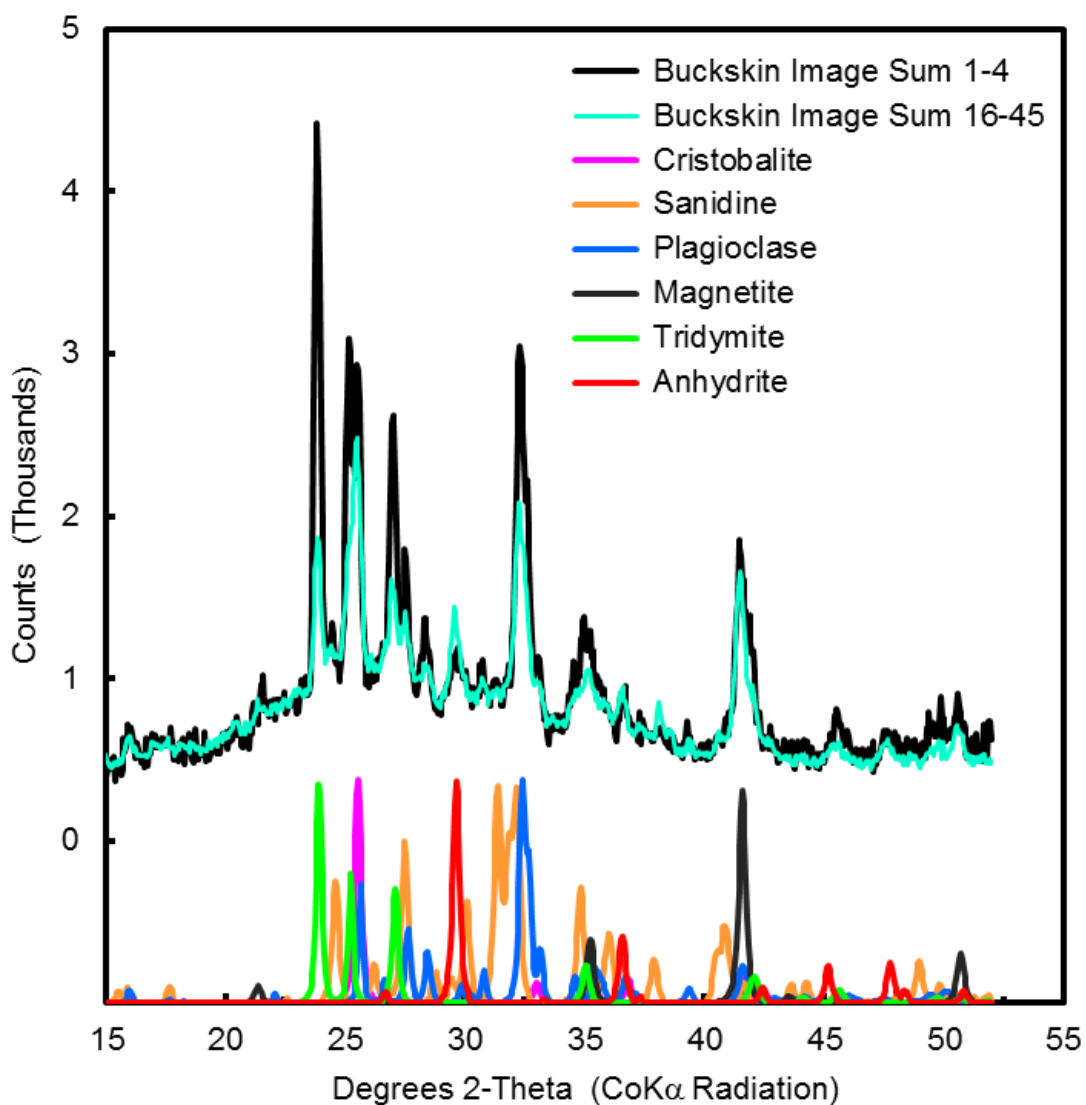
Fig. S3. Comparison of Buckskin patterns from the sum of diffraction images 1-4 and 16-45. Both patterns are normalized to 45 total images (i.e., the same integration time). The diffraction peaks for tridymite and anhydrite decrease and increase in intensity, respectively, in pattern 16-45 versus 1-4. Diffraction patterns for individual crystalline minerals are shown at the bottom of the figure (offset and the most intense peak of each pattern normalized to the same value).
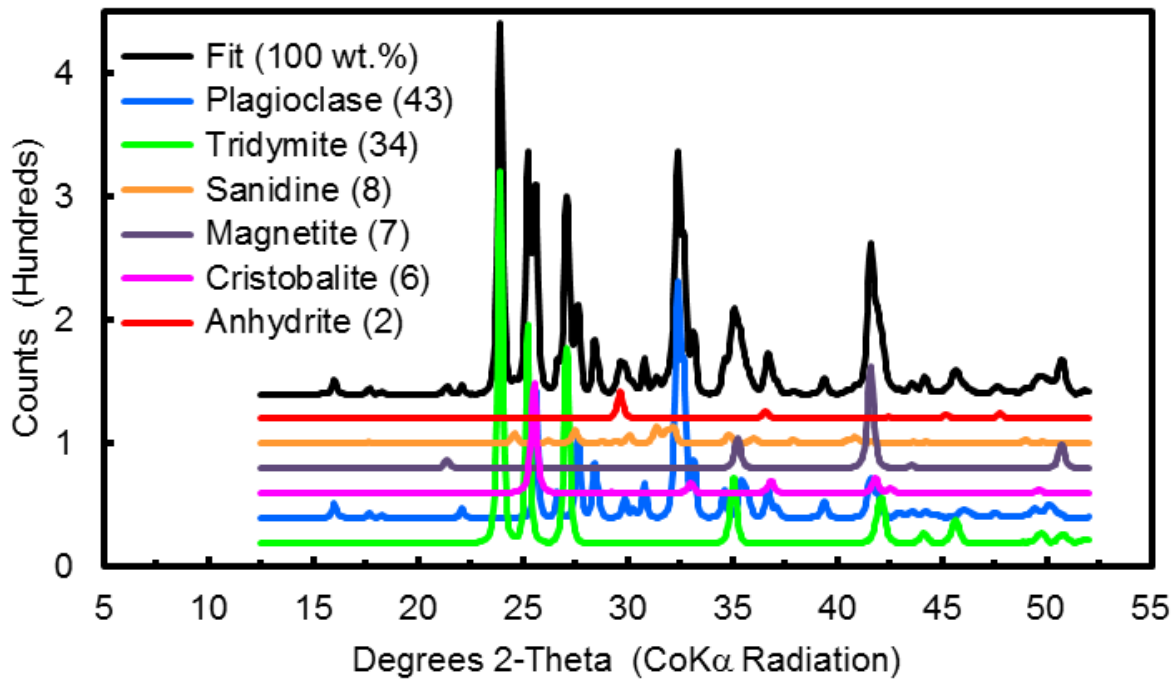
Fig. S4. Individual diffraction patterns for each Buckskin crystalline mineral and fit (sum of individual mineral patterns). The unit cell parameters of tridymite, plagioclase, sanidine, and magnetite were refined during the fitting procedure. Weight percentage of each mineral relative to crystalline material is given in parenthesis. Y-axis corresponds to the Fit pattern; other patterns are offset for clarity.
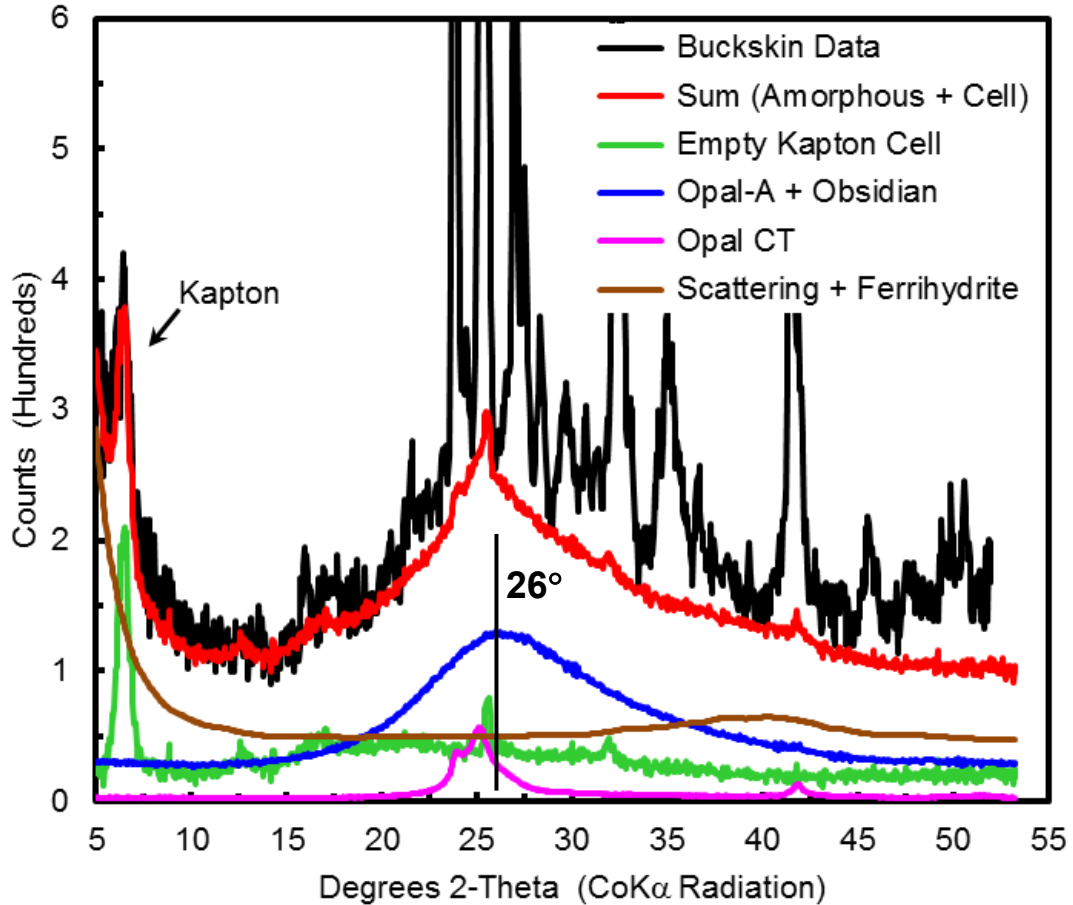
Fig. S5. Diffraction patterns for the sum of amorphous and instrumental components, their individual patterns, and the Buckskin diffraction pattern (sum of diffraction images 1-4). The pattern for opal-A + obsidian was used for purposes of modeling the high-SiO_2 amorphous material, but different combinations of other amorphous high-SiO_2 materials could have been used (e.g., silica glass and rhyolitic glass (Fig. S6)). The peak near 6.5° 2θ is from the Kapton cell window.
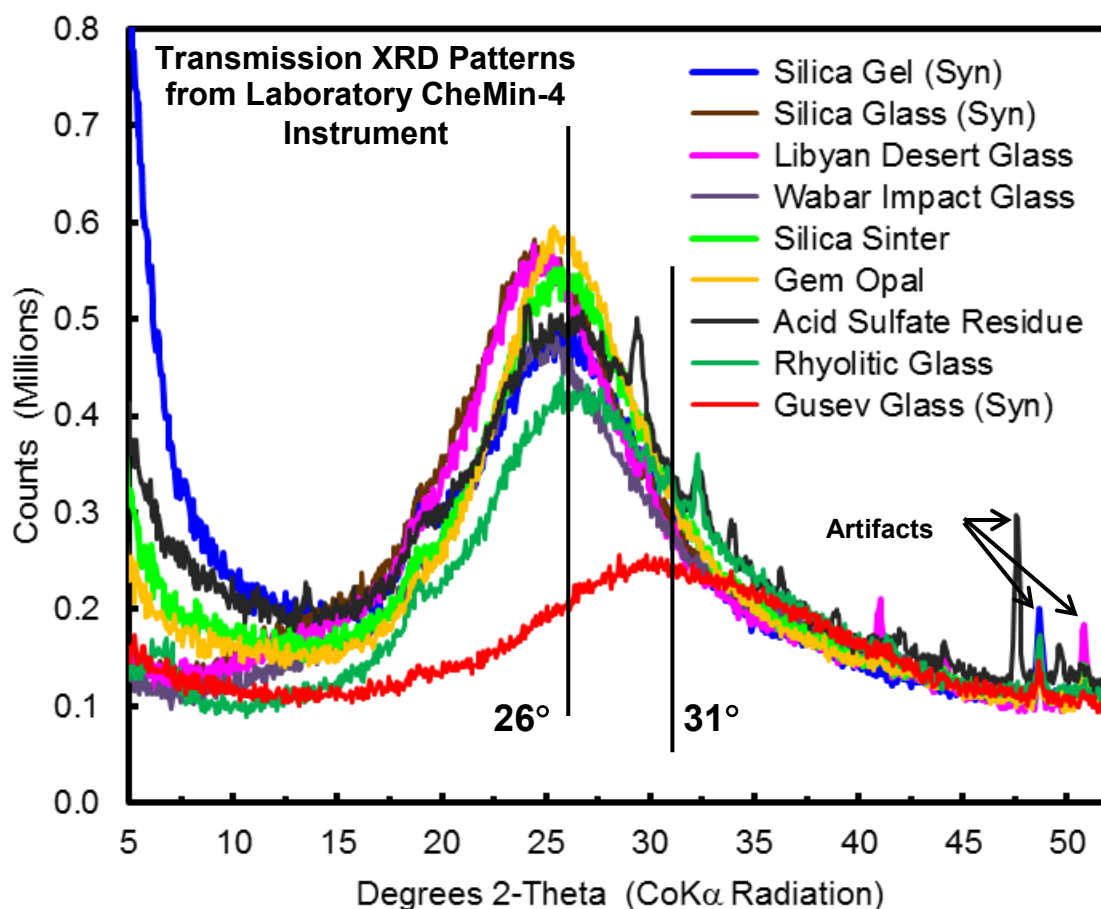
Fig. S6. Transmission XRD patterns for high-silica amorphous materials. Diffraction patterns were obtained on a CheMin-4 instrument that is the laboratory equivalent of the MSL CheMin instrument. Silica gel and silica glass (both synthetic) are nominally 100 wt.% SiO_2 on a water-free basis. Libyan desert glass and Wabar impact glass (Saudi Arabia) are high-SiO_2 glasses formed by meteoritic impact into desert sands. Silica sinter (New Zealand), gem opal (Australia), and the residue of acid-sulfate leaching (Hawaii) all have diffuse diffraction peaks centered near 26° 2θ equivalent to opal-A or synthetic SiO_2 glass. The position of the diffraction peak maximum increases with decreasing SiO_2 concentration from rhyolitic (New Mexico) to ~31° 2θ for Gusev basaltic glass (synthetic). The acid-sulfate residue and the rhyolite patterns have minor diffraction peaks from anatase and quartz, respectively. Gusev glass was used as the model for the amorphous material for Rocknest soil and the John Klein, Cumberland, and Windjana drill samples (7-9). Peaks denoted by arrows are instrumental artifacts.